Available online at www.sciencedirect.com
ScienceDirect
Ceramics International 37 (2011) 2411–2421
CERAMICS INTERNATIONAL
www.elsevier.com/locate/ceramint

# Microstructural relationship with fracture toughness of undoped and rare earths (Y, La) doped $Al_2O_3$–$ZrO_2$ ceramic composites

Kuntal Maiti, Anjan Sil *

*Department of Metallurgical and Materials Engineering, Indian Institute of Technology Roorkee, Roorkee 247 667, Uttarakhand, India*

Received 22 June 2010; received in revised form 2 February 2011; accepted 23 March 2011
Available online 27 May 2011

**Abstract**

Ceramic composites in undoped $Al_2O_3$–5 wt% $ZrO_2$ (AZ) and doped with rare earth elements Y, La separately and simultaneously were prepared by solid state sintering process. These composites were characterized for microstructural investigation and determination of phase formation to draw a possible relationship between these characterization results with the fracture toughness measured by single-edge precracked beam (SEPB) test method using three-point bend test. The fracture toughnesses of Y and Y + La doped AZ are found to be higher for samples sintered at 1700 °C for long soaking times, than that of La doped and undoped AZ composites. It is predicted from the XRD and EDS analyses that the phases of $Zr_{0.88}Y_{0.12}O_{1.94}$ and $Zr_{0.935}Y_{0.065}O_{1.968}$ are formed at or near the intergranular region and therefore the higher fracture toughness of Y and Y + La doped AZ composites compared to undoped AZ and La doped AZ composite for samples sintered at 1700 °C for long soaking times, is attributed to these intergranular phases.


*Keywords:* B. Composites; D. $Al_2O_3$; Rare earth; Fracture toughness

## 1. Introduction

$Al_2O_3$ can be considered as a typical representative of the engineering ceramics. The properties of this ceramic are particularly attractive for structural applications such as in motor, aerospace and biomedical fields, especially when the environmental conditions are particularly severe [1]. The brittleness and poor damage tolerance have limited the scope of almost all the ceramic materials for their use as advanced engineering materials [2]. The fracture toughness of the ceramic materials is generally low because the dislocation motion in the material is extremely limited due to the nature of the chemical bonds which are ionic and/or covalent. The problem of the low fracture toughness of the ceramics can be overcome by designing and preparing the composite materials reinforced with fibres, whiskers and particulates of the same phase as that of matrix or of different suitable phase. The use of $ZrO_2$ based ceramics is one of the possible alternatives to circumvent the limitation of the low fracture toughness [3–5].

The addition of $ZrO_2$ to the $Al_2O_3$ ceramics may increase the fracture toughness of the ceramic composite materials. This effect is based on the tetragonal to monoclinic phase transformation of $ZrO_2$, accompanied by an increase in the specific volume of the order of 3–6%. This volume increase generates a compressive stress in the ceramic matrix near the interface between $ZrO_2$ and $Al_2O_3$, which makes the propagation of crack difficult [6]. This stress-induced phase-transformation toughening and micro-crack toughening are the major toughening mechanisms in $Al_2O_3$–$ZrO_2$ (ZTA) composites [7]. The major applications of ZTAs are in metal cutting tool, wear components, bearings and joint implants [8,9]. The introduction of small amount of $ZrO_2$ as an additive into the $Al_2O_3$ causes the formation of solid solution as can be seen in the $Al_2O_3$–$ZrO_2$ phase diagram given in Fig. 1 [10,11]. This solid solution promotes the densification of the $Al_2O_3$-based composites by the introduction of lattice defects [12–14].

In the present article rare earth doped $Al_2O_3$–5 wt% $ZrO_2$ based ceramic composites are investigated for microstructural development and its correlation with fracture toughness and hardness of the material. To improve the microstructural

* Corresponding author. Tel.: +91 1332 285073; fax: +91 1332 285243/273560.
*E-mail address:* anj_sil@yahoo.co.uk (A. Sil).

0272-8842/$36.00 
doi:10.1016/j.ceramint.2011.05.089

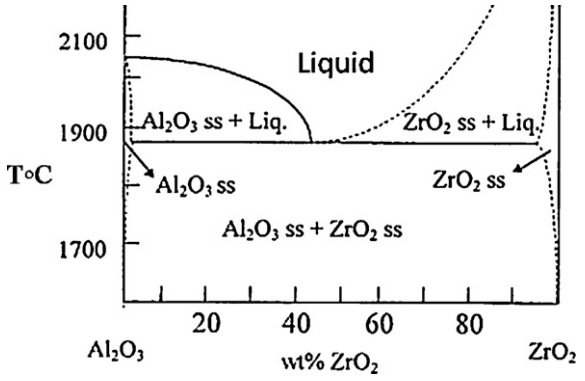


Fig. 1. Phase diagram of the $Al_2O_3$–$ZrO_2$ system. [Levin E.M., 1975].

characteristics and thereby leading to the better mechanical properties, $Al_2O_3$–$ZrO_2$ matrix was chosen to examine the effect of dopants on this composite matrix. This is in view of the fact that such matrix has better densification characteristics than pure $Al_2O_3$ as reported in the literature [8,15–17]. The effect of rare earth elements doping into single oxide such as $Al_2O_3$ ceramics on the mechanical properties has been investigated by various researchers [18,19]. Rani et al. reported the effect of rare earth dopants $Yb^{3+}$, $Er^{3+}$ and $La^{3+}$ on the improvement of room temperature mechanical properties of the $Al_2O_3$. The doped materials sintered at low temperature (1400 °C) are less toughened with fine-equiaxed grains. A noticeable morphologic modification was occurred for the samples sintered at higher sintering temperature. Due to the preferential segregation of the rare earth ions to basal planes (0 0 0 1) in $Al_2O_3$ grain boundaries [20], there is a tendency for the growth of anisotropic elongated grains which facilitates improvement in toughness [21]. An advanced rare earth Y reinforced $Al_2O_3$/(W,Ti)C ceramic composite material was developed and the microstructure, mechanical properties and the cutting performance of the material were reported by Xu et al. The improvement in fracture toughness of this material has been viewed as through the formation of the complex rare earth compounds which increases the binding strength of the interfaces [22]. $Al_2O_3$–5 vol% SiC particle composites doped with 800 ppm rare earth impurities $Y^{3+}$, $Nd^{3+}$ and $La^{3+}$ were prepared by Deng et al. The fracture mode was found to change due to the rare earth doping from transgranular in dopant free composites to the intergranular in the doped composites. The intergranular fracture in the rare earth doped composites is believed to originate from a weak $Al_2O_3$ boundary bonding caused by the segregation of rare earth dopants [23]. Therefore there are no convergent views proposed by the researchers to explain the fracture toughness behaviour of the rare earth doped $Al_2O_3$ based or alike ceramics. Moreover the rare earth doping in the structural ceramic materials leads in general to modify the mechanical properties including creep, fracture toughness, strength, etc. [21]. Therefore there is a need to carry out further investigations towards determining the underlying mechanism of the property modification. Besides proposing the possibility of segregating the rare earth ions at the grain boundaries in the $Al_2O_3$ based ceramics, no other concrete views have, so far, been put forward to explain the fracture toughness behaviour. There is a considerable literature on the microstructure–mechanical properties relationships. The literature on the grain size and second phase particle size effects on mechanical properties was summarized by Rice [24]. In the present work an attempt has been made to investigate the microstructural development of the rare earth doped $Al_2O_3$-based ceramic along with identifying any secondary phases that may generate during the sample preparation by solid state sintering and relating these aspects with the fracture toughness behaviour of the samples prepared with different type of rare earth doped samples.

In order to fulfill the objective, two types of single rare earth doped and one type of rare earths co-doped $Al_2O_3$–5 wt% $ZrO_2$ ceramic composites were prepared. The doping elements Y and La were considered for the present study. Single doped samples were prepared with 1000 ppm Y and 1000 ppm La, whereas, the co-doped sample was prepared with 1000 ppm each of Y and La.

The influence of the sintering temperature and the soaking time period on the microstructural characteristics and the fracture toughness of undoped and rare earth doped (singly and jointly with Y, La) $Al_2O_3$–5 wt% $ZrO_2$-based ceramic composites was investigated. The composite samples were prepared by ceramic powder processing followed by sintering the green compacts at 1500 °C, 1600 °C and 1700 °C for different soaking time periods, viz., 3 h, 6 h, 9 h and 12 h. The fracture toughness and hardness of each sample were determined at room temperature. The other parameters, viz., the density and linear shrinkage of the sintered samples which also depend on the sintering temperature and the soaking time periods were also determined.

## 2. Experimental procedure

The raw materials used are the powders of $Al_2O_3$ (99.8%, 0.4 μm), $ZrO_2$ (99%, 0.4 μm), $Y(NO_3)_3{\cdot}6H_2O$ (99.99%) and $La(NO_3)_3{\cdot}6H_2O$ (99.99%). The incorporation of rare earth ions $Y^{3+}$ and $La^{3+}$ into the $Al_2O_3$–5 wt% $ZrO_2$ mixture was done by adding the nitrates, i.e., $Y(NO_3)_3{\cdot}6H_2O$ and $La(NO_3)_3{\cdot}6H_2O$ to the slurries of the $Al_2O_3$–5 wt% $ZrO_2$. The rare earth doped samples were prepared in the systems of $Al_2O_3$–5 wt% $ZrO_2$–1000 ppm $Y(NO_3)_3{\cdot}6H_2O$, $Al_2O_3$–5 wt% $ZrO_2$–1000 ppm $La(NO_3)_3{\cdot}6H_2O$ and $Al_2O_3$–5 wt% $ZrO_2$–1000 ppm $Y(NO_3)_3{\cdot}6H_2O$–1000 ppm $La(NO_3)_3{\cdot}6H_2O$, which have been described in this article by AZY, AZL and AZLY, respectively. The different powders of required quantities for each system were dispersed in distilled water by the ultrasonication method which deagglomerates the powders. The sonication was done for 6 h with each system. The deagglomerated powders were mixed for 36 h by using magnetic stirrer. The powder mixtures were then dried at 100 °C for 12 h. The dried mixture was further ground lightly in an alumina mortar and pestle. The binder polyvinyl alcohol was added to the ground powder mixture and the granulation was done.

The green powder compacts in the form of rectangular bar having dimension of 3 mm × 5 mm × 45 mm were prepared from the granulated powder mixture using uniaxial hydraulic press at different loads ranging between 15 × 10 kN and 22.5 × 10 kN. The samples were sintered at 1500 °C, 1600 °C and 1700 °C for the soaking time periods of 3 h, 6 h, 9 h and 12 h. The rate of heating as well as cooling was programmed at 10 °C/min for the sintering process. However, the cooling was occurred by the natural furnace cooling. Linear shrinkages of the samples were measured by digital vernier caliper. The density of all the samples was measured following Archimedes principle using water as an immersion medium. The relative densities of the samples were determined based on the theoretical densities estimated following the rule of mixture (ROM) for the ceramic composites prepared. One face of each sample was ground using SiC papers of # 120, # 220, # 320 mesh sizes to prepare good surface finish. The ground surfaces of the samples were polished with 6 and 3 μm sized diamond pastes, to the level of mirror like surface finish. The polished surfaces were indented in Vickers hardness tester with various loads of 5, 10, 15, 20, 30 and 40 kg for fixed dwell time of 15 s at ambient condition. The diagonals of the square shaped indentation were measured by optical microscope (Axiovert 200 MAT, ZEISS). The hardness ($H_v$) of the samples was calculated from the following equation:

$$H_v = \frac{P}{A} = \frac{\alpha P}{d_o^2} \quad (1)$$

where $P$ is the applied load, $A$ is the pyramidal contact area of the indentation, $d_o$ is the average length of the diagonals of the resultant impression and $\alpha = 1.8544$ for Vickers indenter.

The fracture toughness of the rectangular samples was determined by single-edge precracked beam (SEPB) test method using three-point bend test with 20 mm span between the two supports and the cross head speed of 0.5 mm/min. The precrack length is between $0.20W$ and $0.30W$, where $W$ is the height of the test specimen. The sintered samples were characterized for phase identification by X-ray diffractometer (Bruker AXS) using Cu Kα radiation. The X-ray scan rate used was $1^\circ$ $min^{-1}$ and the scanning was done over the angular range of $2\theta = 10$–$90^\circ$.

In order to know the grain structure in the sintered samples, the microstructures were observed by field emission scanning electron microscope (FESEM). The polished surface of the samples was gold coated for the microstructural investigation. The grain size and the porosity of the sintered samples were measured by using Image J software.

## 3. Results and discussion

### 3.1. Microstructural analysis

The different ceramic systems investigated are AZ, AZY, AZL and AZYL. Further the sintering parameters, i.e., temperature (°C) and soaking time period (h) used are specified in the sample descriptions as superscript and subscript, respectively. The description $AZ_3^{1500}$ for example represents the $Al_2O_3$–5 wt% $ZrO_2$ ceramic composite sintered at 1500 °C for the soaking time period of 3 h.

Fig. 2(a)–(d) shows the SEM micrographs of AZ sample sintered at 1500 °C, 1600 °C and 1700 °C for different soaking time periods. The overall increase in grain size with the increasing sintering temperature and soaking time period, is found to occur. The microstructure of the sample given in Fig. 2(a), consists broadly two types of grain structures. The smaller grains have nearly round shape and larger grains have irregular geometry including elongated shape. The average grain size of the sample varies between 0.5 and 5.1 μm. Fig. 2(b) shows that the sample consists of grains of varying sizes from as low as 1.7 to as high as 36.0 μm. The very small sized grains are situated at the intergranular and the triple junctions of the larger grains. As evident from the phase diagram of $Al_2O_3$–$ZrO_2$, the solid solubility of the $ZrO_2$ in the $Al_2O_3$ is low and therefore the excess amount of the 5 wt% $ZrO_2$ used exists as a separate phase within the $Al_2O_3$ matrix. In order to know the possible locations of the $ZrO_2$ particles, microanalysis of one sample $AZ_3^{1700}$ as a typical representative of the AZ ceramic composites, by EDS was carried out. While the point scan on the grain shaded grey shows the presence of the Al and O with negligible amount of Zr, the signals from the tiny bright particles located at the triple junctions of the $Al_2O_3$ grains are from Zr and O with a negligibly small signal from Al. The EDS spectra along with the micrograph is shown in Fig. 2(c) which can confirm that the $ZrO_2$ grains are located at the triple junctions. The grain size variation in Fig. 2(c) is 2.2–39.9 μm. Fig. 2(d) shows the grain structure of the sample $AZ_6^{1700}$. It is appeared from the micrograph that the particles at the triple junctions are relatively larger compared to that in the samples $AZ_3^{1700}$. The grain size for this sample $AZ_6^{1700}$ ranges between 4.3 and 49.8 μm.

Fig. 3(a) shows the micrograph of the sample $AZY_6^{1500}$ for which the grain size range is 0.4–2.9 μm. There is a substantial change in the grain structure developed in the samples $AZY_6^{1600}$, $AZY_3^{1700}$ and $AZY_6^{1700}$ as shown in Fig. 3(b)–(d), respectively, compared to that of the sample $AZY_6^{1500}$ (Fig. 3(a)). It is further evidenced that the triple junctions are occupied by tiny bright particles which are of $ZrO_2$ as already found by the microanalysis of one sample given in Fig. 2(c). The microanalysis of the sample $AZY_3^{1700}$ shows Y content (0.26 at%) is higher at the grain boundary compared to that (0.00 at%) in the grain interior. The Al, O and trace amount of Zr in the EDS spectra obtained both at the grain interior and near the grain boundary are also shown in the elemental analysis data. XRD analysis was carried out for one sample $AZY_6^{1700}$. On examination of the micrographs given in Figs. 2 and 3, it has been found that the Y doping influences the grain growth to cause inhibition. The grain size of the sample $AZY_6^{1600}$ varies between 1.8 and 27.7 μm, the range is lower than that for the sample $AZ_6^{1600}$ for which the grain size range is 1.7–36.0 μm. The grain size of the sample $AZY_3^{1700}$ varies between 2.4 and 29.9 μm and that of $AZY_6^{1700}$ has a range of 2.8–33.0 μm. In contrast, the grain size ranges of $AZ_3^{1700}$ and $AZ_6^{1700}$ are 2.2–39.9 μm and 4.3–49.8 μm, respectively. As

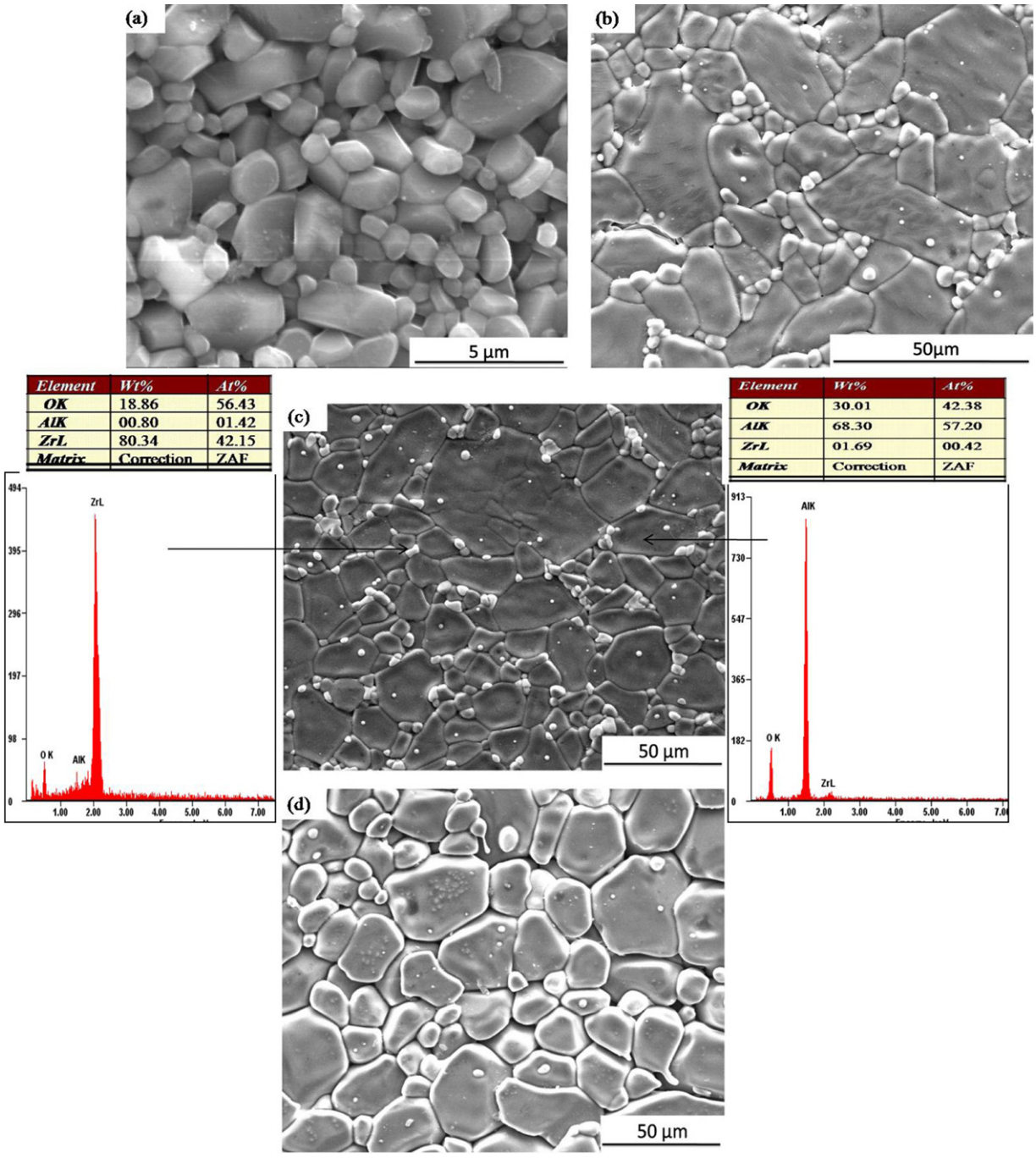


Fig. 2. SEM micrograph of (a) $AZ_6^{1500}$, (b) $AZ_6^{1600}$, (c) $AZ_3^{1700}$ with EDS and (d) $AZ_6^{1700}$ composite samples.

indicated in the XRD pattern (Fig. 7(c)), the dopant Y is present primarily in the form of the compound $Zr_{0.88}Y_{0.12}O_{1.94}$, therefore, it may be assumed that the grain growth inhibition is effected by the presence of this compound [25,26].

In Fig. 4(a) the grains in the sample $AZL_6^{1500}$ have round shape and are nearly uniform in size which varies from 0.4 to 3.1 μm. However, an extensive grain growth is observed for the sample $AZL_6^{1600}$, the grain size variation of which is 2.1–36.1 μm. The microstructure is similar to the AZ samples given in Fig. 2. However, for the La doped samples, unlike Y doped samples, the rare earth (La) content at or near the grain boundary phase is less (0.11 at%) compared to that (0.25 at%) in the grain interior.

Fig. 4(a)–(c) shows relatively compact grain structure compared to the case shown in Fig. 4(d). Figs. 2(d) and 4(d) have similar microstructure. The grain size ranges for the samples $AZL_3^{1700}$ and $AZL_6^{1700}$ are 2.4–39.1 μm and 3.9–46.5 μm, respectively. AZL samples have higher grain size than AZY. Fig. 4(c) shows the FESEM micrograph and EDS results of the sample $AZL_3^{1700}$. The EDS spectra obtained from the grain interior surface and near grain boundaries of $Al_2O_3$ show the presence of La along with other major elements Al, Zr and

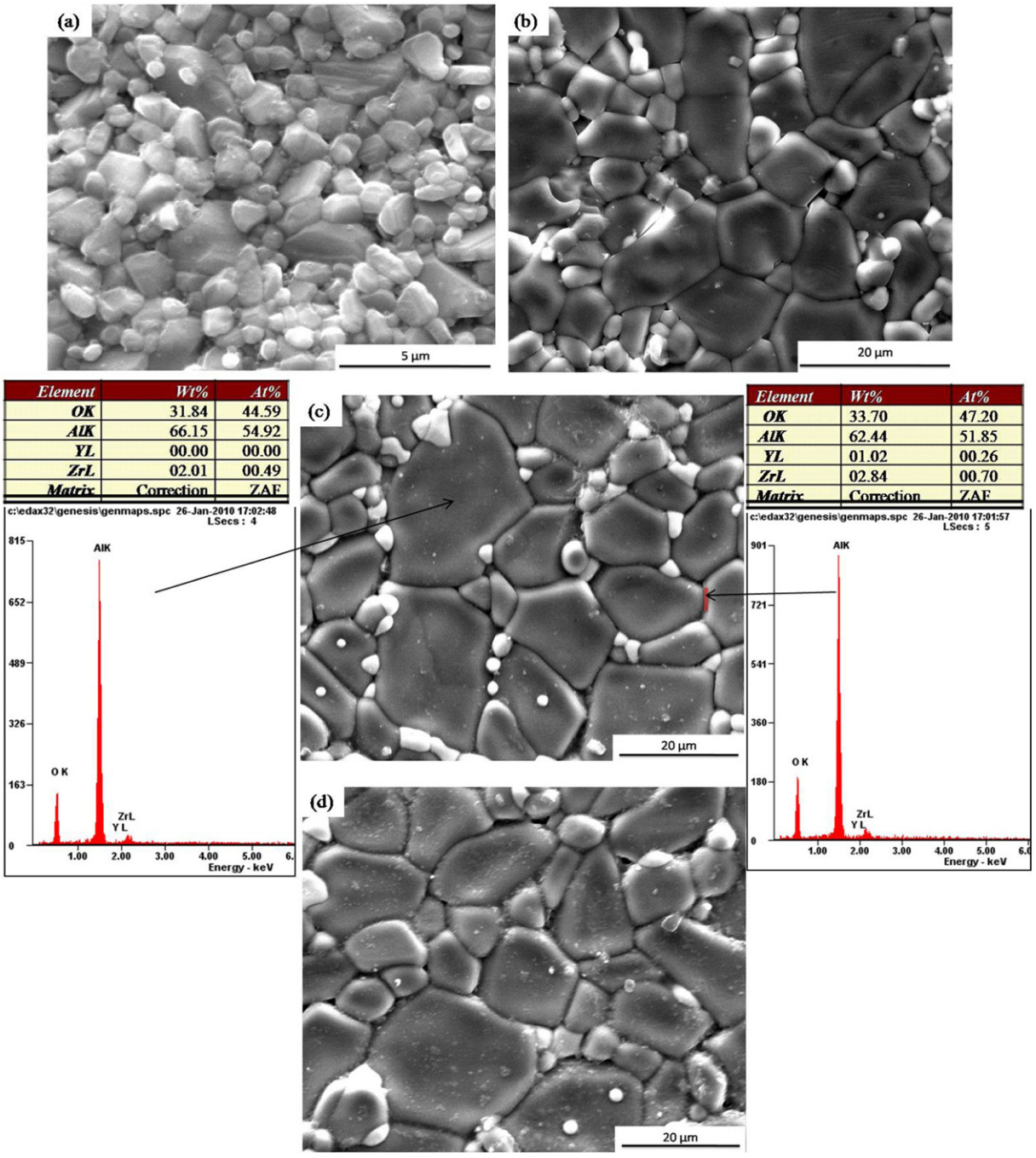


Fig. 3. SEM micrograph of the sample: (a) $AZY_6^{1500}$, (b) $AZY_6^{1600}$, (c) $AZY_3^{1700}$ with EDS and (d) $AZY_6^{1700}$.

O. XRD analysis of La doped material was carried out for one sample $AZL_6^{1700}$.

Fig. 5(a) of $AZYL_6^{1500}$ consists of the smaller round shaped grains and a few larger grains of largely elongated type. The grain size in the sample $AZYL_6^{1500}$ varies between 0.4 and 3.1 μm and in Fig. 5(b) of $AZYL_6^{1600}$, the range is 1.6–26.4 μm. Fig. 5(b)–(d) shows the larger grains are of $Al_2O_3$ and smaller grains shaded white are of $ZrO_2$. The grain size ranges for the samples $AZYL_3^{1700}$ and $AZYL_6^{1700}$ are 2.4–31.9 μm and 4.5–33.4 μm, respectively. The EDS spectra obtained from the grain interior surface of $ZrO_2$ and near grain boundaries of $Al_2O_3$ show the presence of $Y^{3+}$ along with other major elements Al, Zr and O (Fig. 5(c)).

### 3.2. XRD analyses

Fig. 6 shows the XRD patterns of the samples $AZ_6^{1700}$ and $Al_2O_3$ ($A_6^{1700}$). While all the peaks in the pattern for $A_6^{1700}$ sample belongs to $Al_2O_3$ (ICDD file No. 00-046-1212), the pattern for the sample $AZ_6^{1700}$ consists the phases of $Al_2O_3$, $Al_{0.18}Zr_{0.82}O_{1.91}$ and $ZrO_2$ (ICSD file Nos.01-071-1127, 00-053-0572 and 01-074-1201, respectively). The patterns over the

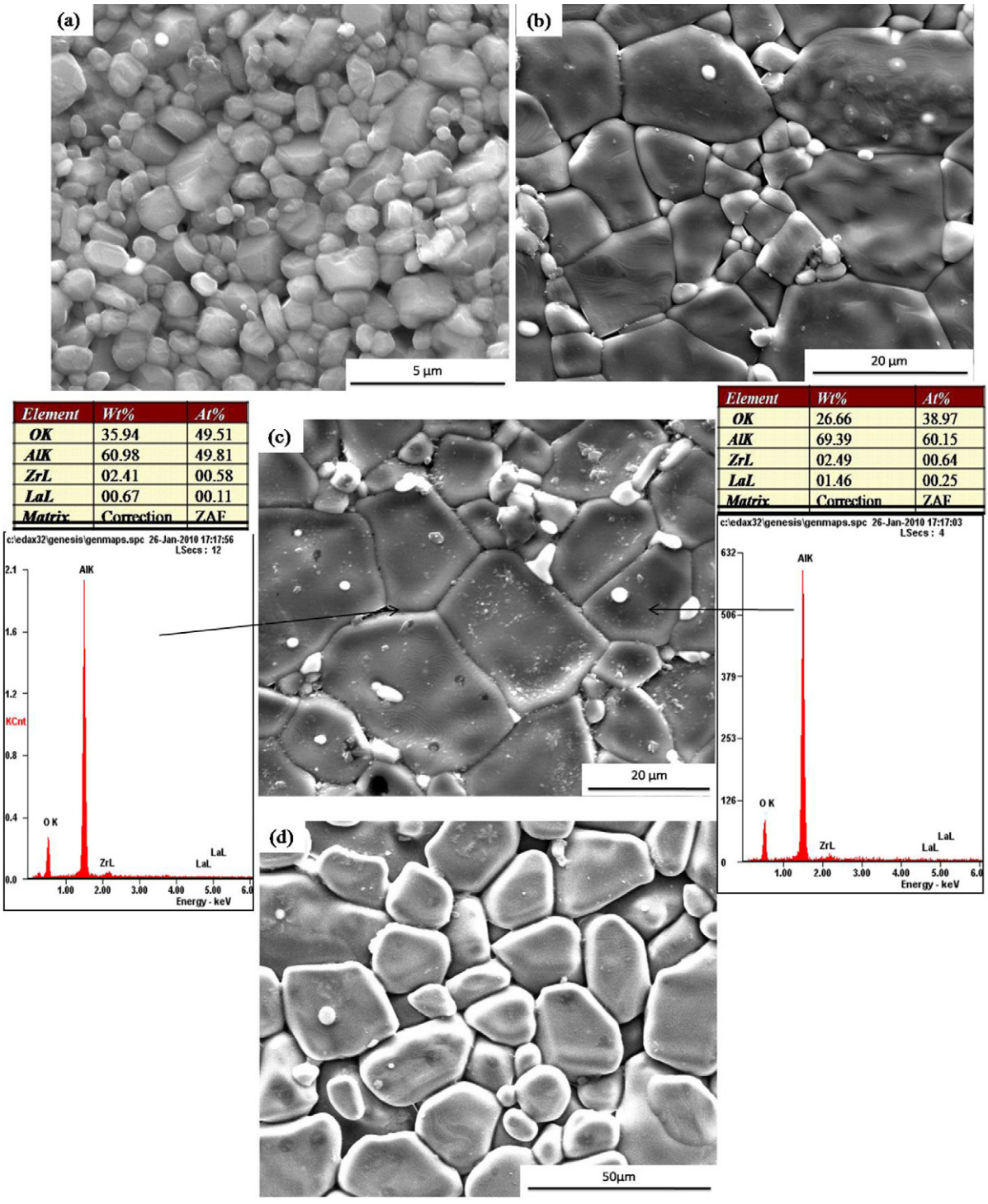


Fig. 4. SEM micrograph of (a) $AZL_6^{1500}$, (b) $AZL_6^{1600}$, (c) $AZL_3^{1700}$ with EDS and (d) $AZL_6^{1700}$.

angular range of $2\theta$ between 22° and 36° are shown separately in Fig. 7. The appearance of the peaks for $AZ_6^{1700}$ over this angular range was also reported by other researchers [4,27,28]. The XRD pattern of $AZY_6^{1700}$ composite is shown in Fig. 7(c), the phase of $Zr_{0.88}Y_{0.12}O_{1.94}$ (ICSD data file No. 01-082-1242 with highest intensity peak) is present along with $ZrO_2$ and $Al_2O_3$ phases [29]. The XRD pattern of $AZL_6^{1700}$ composite is shown in Fig. 7(d), the phases of $Al_{0.01}Zr_{0.99}O_{1.99}$ (ICDD data file No. 00-053-0548) and $La_{0.9}Al_{11.76}O_{19}$ along with $ZrO_2$ and $Al_2O_3$ are present. The peak height of 100% intensity for the compound $Al_{0.01}Zr_{0.99}O_{1.99}$ is negligibly small. XRD analysis of the co-doped (with Y + La) material was carried out for one sample of $AZYL_6^{1700}$.

The XRD pattern (Fig. 7(e)) of $AZYL_6^{1700}$ composite shows the formation of $Zr_{0.935}Y_{0.065}O_{1.968}$ phase (ICSD file No. 01-078-1808) along with of $LaYO_3$, $Al_3Zr$ and $ZrO_2$ phases.

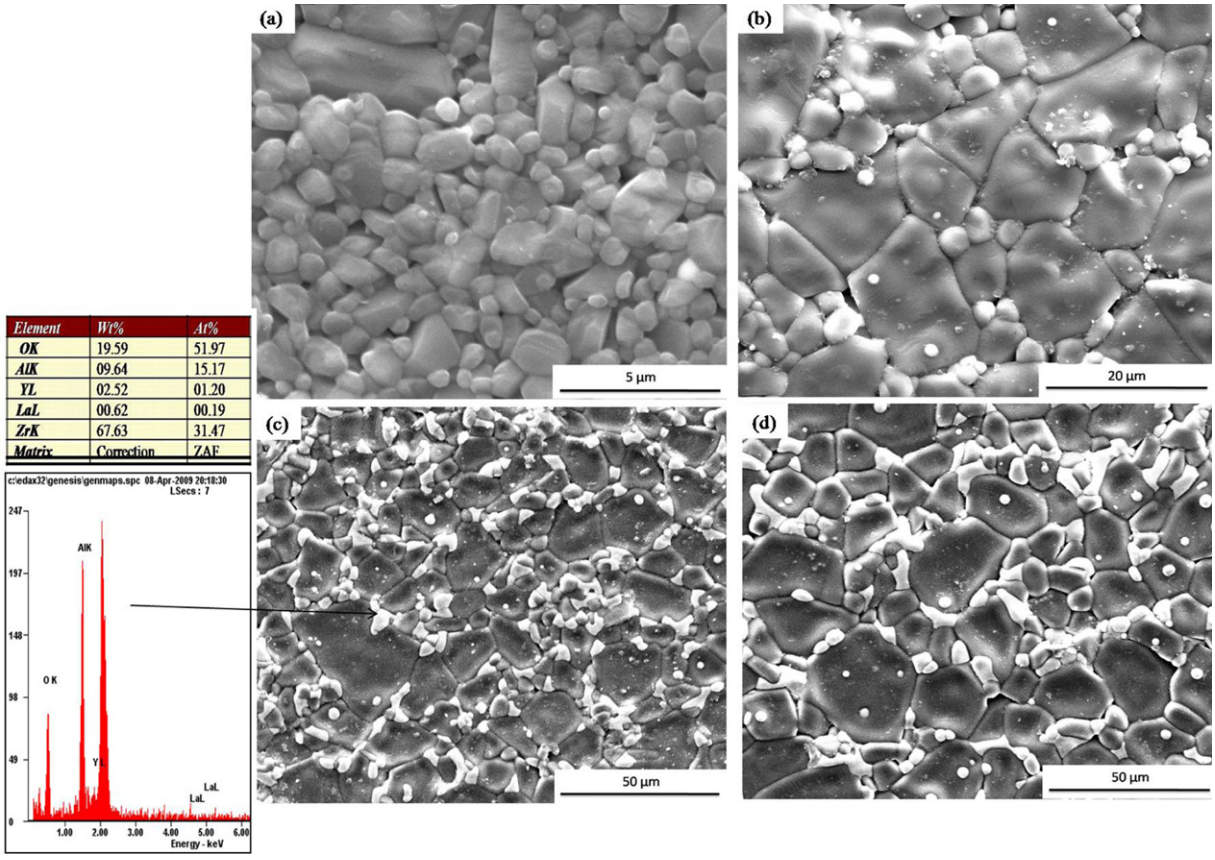


Fig. 5. SEM micrograph of (a) $AZYL_6^{1500}$, (b) $AZYL_6^{1600}$, (c) $AZYL_3^{1700}$ with EDS and (d) $AZYL_6^{1700}$.

The phase $Zr_{0.88}$ $Y_{0.12}O_{1.94}$ being interfacial compound is present in the AZY material in very minute proportion compared to the bulk $Al_2O_3$. Therefore the relative intensity of the XRD peaks of this phase $Zr_{0.88}$ $Y_{0.12}O_{1.94}$ in the pattern is very low which consequently poses difficulty to predict the presence of such phases. In order to establish the predictability of the phases the stoichiometric compound $Zr_{0.88}$ $Y_{0.12}O_{1.94}$ was separately synthesized by the method of mixing of the raw materials $Y_2O_3$ and $ZrO_2$ powders followed by calcinations at 1500 °C for 6 h. The calcined powder was characterized by X-ray diffractometry. The XRD pattern is shown in Fig. 8 which shows the evidence of the formation of chemical compound phase. This control experiment thus confirms the formation of the stated phase in the intergranular region of AZY material.

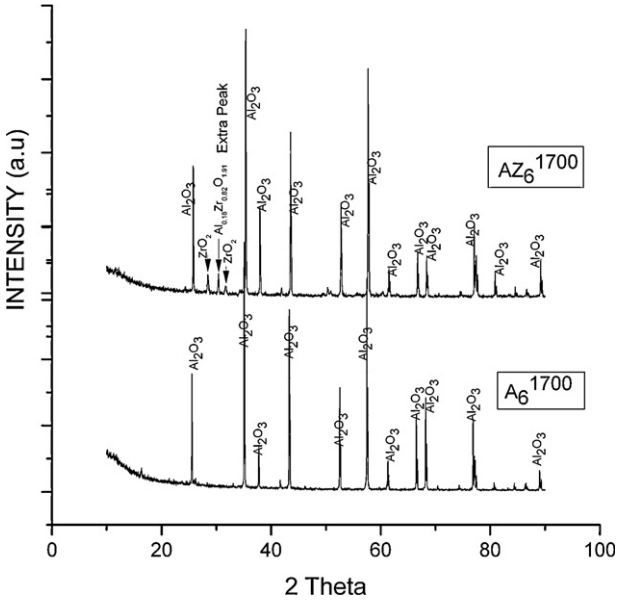


Fig. 6. X-ray diffraction patterns of $A_6^{1700}$ and $AZ_6^{1700}$ samples.

### 3.3. Physical properties

The sintered samples are found to have relatively higher density which varies from 97.0 to 99.3%. Table 2 shows relative densities of the samples sintered at different temperatures for different soaking time periods.

The weight losses (i.e., the difference in weight between the green compact and the sintered sample) of the samples AZ, AZY, AZL and AZYL on sintering at 1500 °C, 1600 °C and 1700 °C are shown in Fig. 9. For the sample AZ sintered at 1500 °C the weight loss as shown in Fig. 9(a), is more than the AZY, AZL and AZYL. But weight loss is less in the sample AZ sintered at 1600 °C and 1700 °C than AZY, AZL and AZYL. The AZL sintered at 1700 °C shows the higher weight loss signifying the formation of more volatile matter thereby leading to lower densification [29]. Chemical reaction or the formation of the compound may promote the weight loss [30]. Therefore

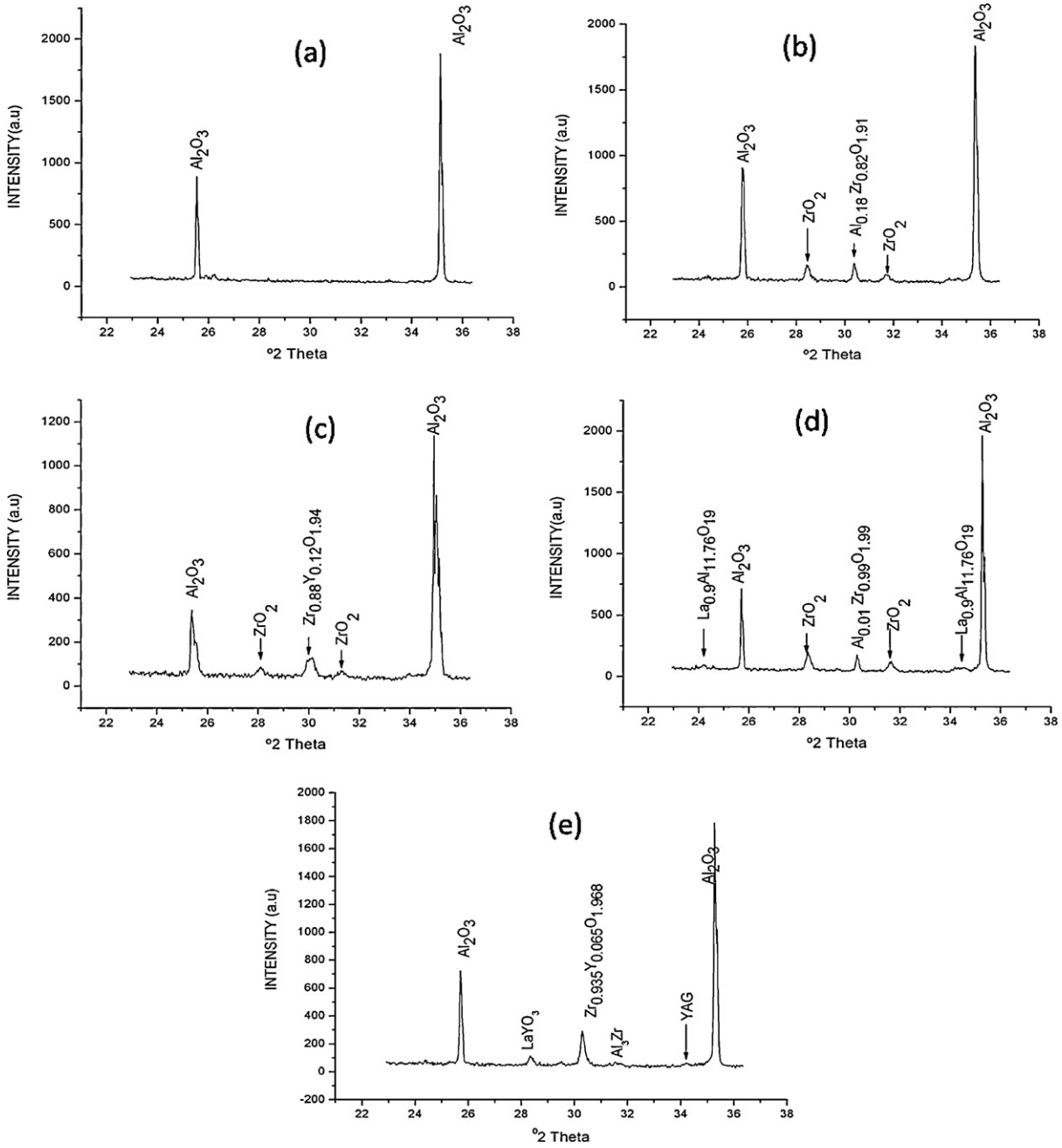


Fig. 7. X-ray diffraction pattern of (a) $A_6^{1700}$, (b) $AZ_6^{1700}$, (c) $AZY_6^{1700}$, (d) $AZL_6^{1700}$ and (e) $AZYL_6^{1700}$.

the porosity development in the samples is also more in these samples which consequently reduces the density of these materials. This causes lower fracture toughness for the samples AZL sintered at 1700 °C which is given in Table 1. But weight loss for the samples AZ sintered at 1700 °C is less which means the formation of volatile material is less. The weight loss in the sample that takes place during sintering is an indicative of the degree of porosity development into the samples [30]. This in turn relates to the fracture toughness of the material. The porosity is susceptible to fracture of the material. The weight loss of the samples due to sintering are estimated from the weight measurements of the samples before and after sintering.

### 3.4. Mechanical properties

Fracture toughness and measured hardness of the samples are listed in Table 1. The hardness of the samples AZ sintered at 1500 °C varies between 12.6 and 15.3 GPa. The samples sintered at 1600 °C and 1700 °C show the hardness varying between 6.3 and 12 GPa and the occurrence of this lower hardness range is attributed to the larger grain sizes of the samples sintered at 1600 °C and 1700 °C compared to the samples sintered at 1500 °C. The AZY, AZL and AZYL samples sintered at 1500 °C and 1600 °C show higher hardness compared to the samples sintered at 1700 °C. The samples AZ and AZY sintered at 1700 °C show higher hardness than that of

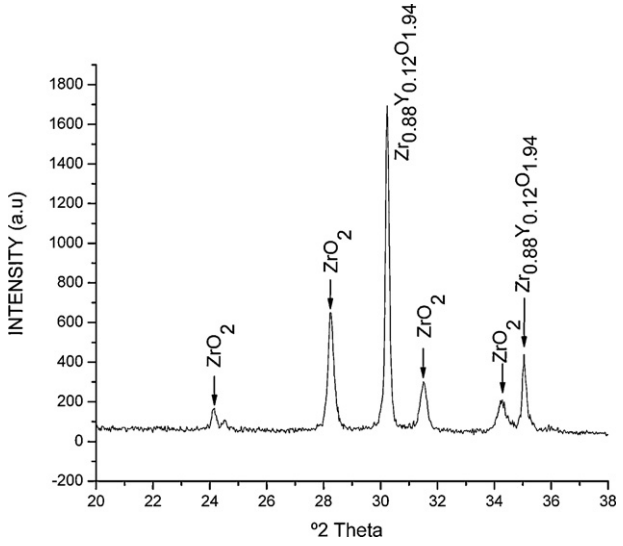


Fig. 8. X-ray diffraction patterns of $ZY_6^{1500}$ sample.

the La doped samples AZL and AZYL. Lower hardnesses were also observed by other researchers. Lu et al. reported the hardness values of 2.26 and 2.09 GPa for pure $Al_2O_3$ and composite of $Al_2O_3$–5 wt% $MgB_2$, respectively [31].

The fracture toughness of the systems AZY and AZYL sintered at 1700 °C for all the soaking periods studied is moderately high. However, the fracture toughness of AZ, AZL systems sintered at 1700 °C for soaking periods of 6 h, 9 h and 12 h is relatively lower. The XRD analysis has shown the formation of the phases $Al_{0.18}$ $Zr_{0.82}O_{1.91}$ and $Al_{0.01}Zr_{0.99}O_{1.99}$ in $AZ_6^{1700}$ and $AZL_6^{1700}$, respectively. The lower fracture toughness of these samples may be attributed to the combined effect of larger grain size [6] and the intergranular phases formed. The lower fracture toughness in the sample $AZ_6^{1700}$ and $AZL_6^{1700}$ can be attributed primarily to the microstructure of non-densified grain structure [24,32]. On the other hand the compound formations of $Zr_{0.88}Y_{0.12}O_{1.94}$ and $Zr_{0.935}Y_{0.065}O_{1.968}$ in the samples $AZY_6^{1700}$ and $AZYL_6^{1700}$, respectively, seem to play an important role in enhancing fracture toughness [33–35]. This observation has not been reported so far.

The probable effect of the compound formation on enhancing the fracture toughness has been predicted considering the fracture toughness behaviour exhibited for the samples sintered at 1700 °C for long sintering time. It is quite clear from Table 1 that for the samples sintered at 1700 °C for soaking time periods of 6, 9 and 12 h, it has been found that fracture toughness of the 1000 ppm $Y(NO_3)_3{\cdot}6H_2O$ doped AZ samples

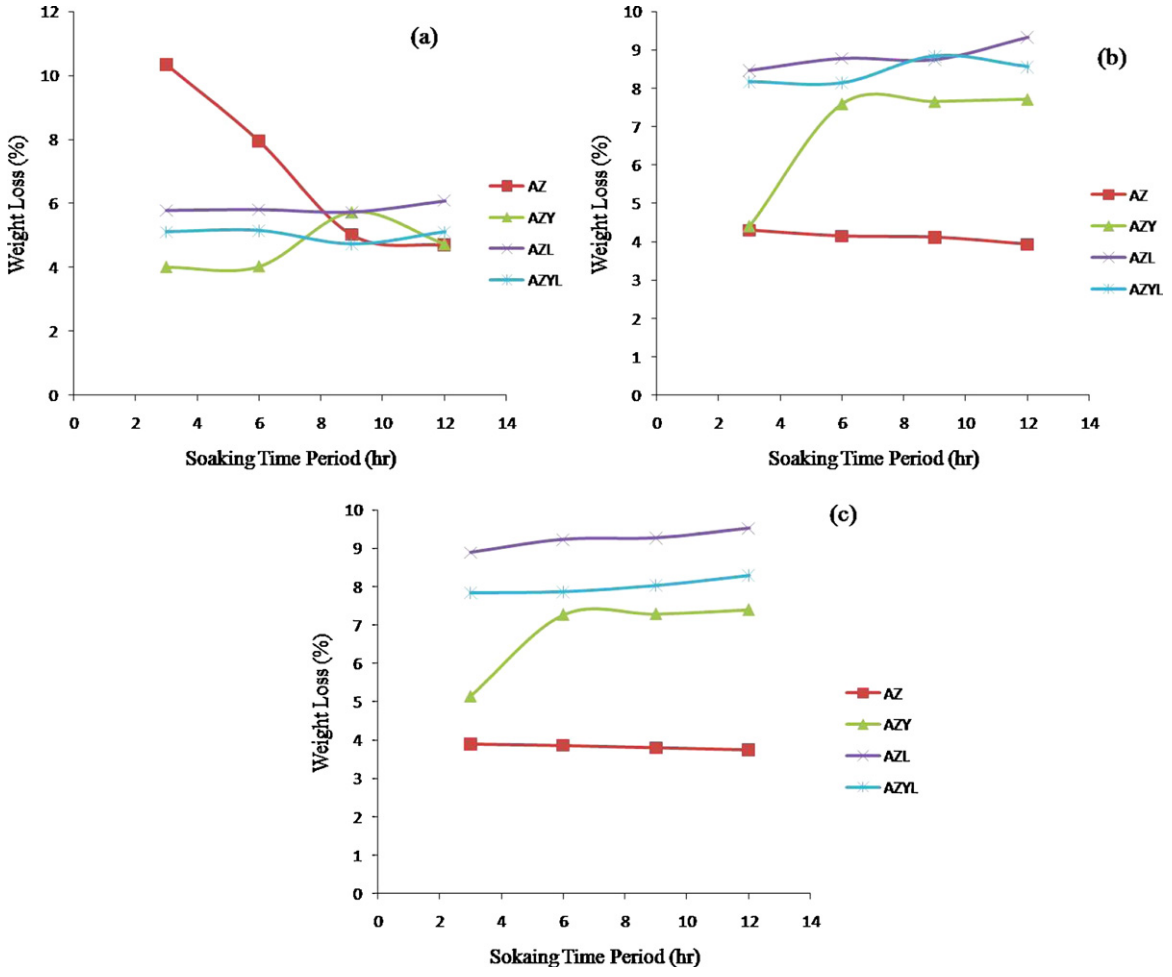


Fig. 9. Weight loss as a function of sintering time of the samples sintered at (a) 1500 °C, (b) 1600 °C and (c) 1700 °C.

Table 1
Fracture toughness and hardness of the AZ, AZY, AZL and AZYL samples sintered at different temperatures and soaking time periods.

| Temp (°C) | Time (h) | AZ | | AZY | | AZL | | AZYL | |
|---|---|---|---|---|---|---|---|---|---|
| | | $H_v$ (GPa) | $K_{IC}$ (MPa $m^{1/2}$) | $H_v$ (GPa) | $K_{IC}$ (MPa $m^{1/2}$) | $H_v$ (GPa) | $K_{IC}$ (MPa $m^{1/2}$) | $H_v$ (GPa) | $K_{IC}$ (MPa $m^{1/2}$) |
| 1500 °C | 3 h | 15.3 | 4.9 | 15.2 | 4.5 | 14.8 | 4.2 | 14.3 | 4.1 |
| | 6 h | 14.5 | 5.3 | 15.0 | 4.7 | 14.0 | 4.3 | 14.0 | 5.1 |
| | 9 h | 13.9 | 5.1 | 13.3 | 4.7 | 14.4 | 4.5 | 13.9 | 4.7 |
| | 12 h | 12.6 | 5.2 | 13.2 | 4.9 | 13.0 | 4.6 | 13.8 | 4.8 |
| 1600 °C | 3 h | 12 | 5.2 | 10.3 | 5.0 | 13.9 | 4.7 | 12.1 | 4.7 |
| | 6 h | 11.2 | 5.2 | 10.4 | 4.7 | 13.4 | 4.9 | 12.5 | 4.9 |
| | 9 h | 9.7 | 5.2 | 10.9 | 4.7 | 12.0 | 4.7 | 12.0 | 5.1 |
| | 12 h | 7.9 | 5.2 | 10.1 | 4.9 | 11.7 | 4.7 | 12.0 | 5.2 |
| 1700 °C | 3 h | 8.2 | 5.2 | 10.7 | 5.3 | 4.0 | 5.3 | 5.3 | 5.5 |
| | 6 h | 7.3 | 1.9 | 9.2 | 5.0 | 4.3 | 2.1 | 5.0 | 5.0 |
| | 9 h | 5.8 | 1.7 | 9.0 | 5.2 | 4.1 | 1.8 | 5.1 | 4.9 |
| | 12 h | 6.3 | 1.7 | 8.3 | 4.5 | 4.1 | 1.8 | 4.9 | 4.5 |

Table 2
Relative densities of AZ, AZY, AZL AZYL samples sintered at 1500 °C, 1600 °C and 1700 °C for different soaking time periods.

| Temperature (°C) | 1500 °C | | | | 1600 °C | | | | 1700 °C | | | |
|---|---|---|---|---|---|---|---|---|---|---|---|---|
| Soaking time (h) | 3 h | 6 h | 9 h | 12 h | 3 h | 6 h | 9 h | 12 h | 3 h | 6 h | 9 h | 12 h |
| Relative density (%) | | | | | | | | | | | | |
| AZ | 97.3 | 97.5 | 98.3 | 98.3 | 98.01 | 98.3 | 98.5 | 98.8 | 98.5 | 98.0 | 97.8 | 97.8 |
| AZY | 98.0 | 98.3 | 98.3 | 97.8 | 99.0 | 99.3 | 99.3 | 99.3 | 99.0 | 99.0 | 98.8 | 98.8 |
| AZL | 97.0 | 97.3 | 97.8 | 98.0 | 98.5 | 98.8 | 98.3 | 98.5 | 98.3 | 98.0 | 98.0 | 97.8 |
| AZYL | 97.5 | 97.8 | 98.0 | 98.5 | 98.5 | 99.0 | 99.3 | 99.3 | 98.5 | 99.0 | 98.5 | 99.0 |

enhances as compared to the undoped AZ samples. It is further noticed doping with (1000 ppm) only of $La(NO_3)_3{\cdot}6H_2O$ in AZ sample does not enhance the fracture toughness value as compared to undoped AZ samples. However, $La(NO_3)_3{\cdot}6H_2O$ co-doping with $Y(NO_3)_3{\cdot}6H_2O$ in AZ enhances the fracture toughness value as compared to undoped AZ samples. On the other hand XRD patterns along with EDS analyses of the undoped and doped AZ samples show the evidence of $Zr_{0.88}Y_{0.12}O_{1.94}$ and $Zr_{0.935}Y_{0.065}O_{1.968}$ compounds formation in the intergranular regions of AZY and AZYL, respectively. Though the XRD and the EDS analyses were carried out on the samples sintered at 1700 °C for a soaking time of 6 h.

## 4. Conclusions

1. The relative densities of all the samples in five different systems of AZ, AZY, AZL and AZYL lie between 96.3 and 99.3%.
2. The segregation of the $ZrO_2$ at the triple junctions and the intergranular regions of the $Al_2O_3$ grains are observed in the system AZ.
3. The tendency for Y segregation as compared to La at the intergranular region is more. This is because the Y forms compound with $ZrO_2$ as established in the AZ system.
4. The compound formations in the intergranular region of the AZ, AZY, AZL and AZYL samples are $Al_{0.18}Zr_{0.82}O_{1.91}$, $Zr_{0.88}Y_{0.12}O_{1.94}$, $Al_{0.01}Zr_{0.99}O_{1.99}$ and $Zr_{0.935}Y_{0.065}O_{1.968}$, respectively.
5. The rare earth dopants are not present as isolated elements in the intergranular region. The elements are absorbed in the compounds formed.
6. The fracture toughness of AZ sintered at 1700 °C for long sintering time (i.e., for 6, 9 and 12 h) is lower and is found to increase for the doped AZY and AZYL samples. Such enhancement in fracture toughness is attributed to the compound formations of $Zr_{0.88}Y_{0.12}O_{1.94}$ and $Zr_{0.935}Y_{0.065}O_{1.968}$, respectively, in the intergranular regions.
7. The fracture toughness of the samples sintered at 1500 °C and 1600 °C for undoped and doped are nearly same. However, the samples sintered at 1700 °C show lower fracture toughness for AZ and AZL sintered for soaking time periods of 6 h, 9 h and 12 h. There is no decrease in fracture toughness for the samples AZY and AZYL sintered at 1700 °C for any of the soaking time periods used.

## References

[1] F. Cesari, L. Esposito, F.M. Furgiuele, C. Maletta, A. Tucci, Fracture toughness of alumina–zirconia composites, Ceram. Int. 32 (2006) 249–255.
[2] Y.L. Dong, F.M. Xu, X.L. Shi, C. Zhang, J.M. Yang, Y. Tan, Fabrication and mechanical properties of nano-/micro-sized $Al_2O_3$/SiC composites, Mater. Sci. Eng. A 504 (2009) 49–54.
[3] D.L. Porter, A.G. Evans, A.H. Heuer, Transformation-toughening in partially-stabilized zirconia (PSZ), Acta Metall. 27 (1997) 1649–1654.
[4] S. Shukla, S. Seal, R. Vij, S. Bandyopadhyay, Z. Rahman, Effect of nanocrystallite morphology on the metastable tetragonal phase stabilization in zirconia, Nano Lett. 2 (9) (2002) 989–993.

[5] T. Kosmac, M.V. Swain, N. Claussen, The role of tetragonal and monoclinic $ZrO_2$ particles in the fracture toughness of $Al_2O_3$–$ZrO_2$ composites, Mater. Sci. Eng. A 71 (1985) 57–64.
[6] J.K.M.F. Daguano, C. Santos, R.C. Souza, R.M. Balestra, K.E.C.N. Strecker, Properties of $ZrO_2$–$Al_2O_3$ composite as a function of isothermal holding time, Int. J. Refract. Met. Hard Mater. 25 (2007) 374–379.
[7] Y.S. Shin, Y.W. Rhee, S.J.L. Kang, Experimental evaluation of toughening mechanisms in alumina–zirconia composites, J. Am. Ceram. Soc. 82 (5) (1999) 1229–1232.
[8] J.M.C. Moreno, A.R.A. Lopez, A.D. Rodriguez, J.L. Routbort, Microstructure and creep properties of alumina/zirconia ceramics, J. Eur. Ceram. Soc. 15 (1995) 983–988.
[9] R.C. Garvie, M.V. Swain, Thermodynamics of the tetragonal to monoclinic phase transformation in constrained zirconia microcrystals, J. Mater. Sci. 20 (1985) 1193–1200.
[10] E.M. Levin, H.F. McMurdie, Fig. 4378, in: M.K. Reser (Ed.), Phase Diagrams for Ceramists, vol. 3, American Ceramic Society, Westerville, OH, 1975.
[11] X. Zhou, V. Shukla, W.R. Cannon, B.H. Kear, Metastable phase formation in plasma-sprayed $ZrO_2$ ($Y_2O_3$)–$Al_2O_3$, J. Am. Ceram. Soc. 86 (8) (2003) 1415–1420.
[12] J. Wang, R. Stevens, Review zirconia-toughened alumina (ZTA) ceramics, J. Mater. Sci. 24 (1989) 3421–3440.
[13] H.P. Cahnoon, C.J. Christensen, Sintering and grain growth of alpha-alumina, J. Am. Ceram. Soc. 39 (10) (1956) 337–344.
[14] M.M.R. Boutz, A.J.A. Winnubst, F. Hartgers, A.J. Burggaaf, Effect of additives on densification and deformation of tetragonal zirconia, J. Mater. Sci. 29 (1994) 5374–5382.
[15] D. Basu, B.K. Sarkar, Effect of zirconia addition on the fatigue behaviour of fine grained alumina, Bull. Mater. Sci. 24 (2) (2001) 101–104.
[16] C.J. Wang, C.J. Huanng, Y.C. Wu, Two step sintering of fine alumina–zirconia ceramics, Ceram. Int. 35 (2009) 1467–1472.
[17] W.H. Tuan, J.R. Chen, C.J. Ho, Critical zirconia amount to enhance the strength of alumina, Ceram. Int. 34 (2008) 2129–2135.
[18] Z. Xihua, L. Changxia, L. Musen, Z. Jianhua, Research on toughening mechanisms of alumina matrix ceramic composite materials improved by rare earth additive, J. Rare Earth 26 (3) (2008) 367–370.
[19] J. Cho, M.P. Harmer, H.M. Chan, J.M. Rickman, A.M. Thompson, Effect of yttrium and lanthanum on the tensile creep behavior of aluminum oxide, J. Am. Ceram. Soc. 80 (4) (1997) 1013–1017.
[20] A. Altay, M.A. Gulgun, Microstructural evolution of calcium-doped α-alumina, J. Am. Ceram. Soc. 86 (4) (2003) 623–629.
[21] D.A. Rani, Y. Yoshizawa, K. Hirao, Y. Yamauch, Effect of rare-earth dopants on mechanical properties of alumina, J. Am. Ceram. Soc. 87 (2) (2004) 289–292.
[22] C. Xu, X. Ai, Particle dispersed ceramic composite reinforced with rare earth additions, Int. J. Refract. Met. Hard Mater. 19 (2001) 85–88.
[23] Z.Y. Deng, Y. Zhou, M.F. Brito, Y. Tanaka, T. Ohji, Effects of rare earth dopants on grain boundary bounding in alumina–silicon carbide composites, J. Eur. Ceram. Soc. 24 (2004) 511–516.
[24] R.W. Rice, Mechanical Properties of Ceramics and Composites: Grain and Particle Effects, Marcel Dekker, New York, 2000.
[25] C.B. Carter, M.G. Norton, Ceramic Materials: Science and Engineering, Springer, New York, 2007.
[26] K.W. Chae, D.Y. Kim, B.C. Kim, B.K. Kim, Effect of $Y_2O_3$ additions on the densification of an $Al_2O_3$–TiC composite, J. Am. Ceram. Soc. 76 (7) (1993) 1857–1860.
[27] Y.Q. Li, J. Xu, T. Qiu, X.C. He, X.M. Sheng, Alumina effect on the phase transformation in vibration ball-milling zirconia (yttria) powders, J. Mater. Sci. Lett. 11 (1992) 669–670.
[28] S. Rajendran, H.J. Rossell, J.V. Sanders, Preparation and characterization of precursor powders for yttria-doped tetragonal zirconia polycrystals (Y-TZP) and Y-TZP–$Al_2O_3$ composites, J. Mater. Sci. 24 (1989) 1195–1202.
[29] M.K. Haldar, T.K. Pal, G. Banerjee, Preparation and properties of $Y_2O_3$ containing zirconia–mullite composites derived from sillimanite beach sand, Ceram. Int. 28 (2002) 311–318.
[30] F. Hue, Y. Jorand, J. Dubois, G. Fantozzi, Analysis of the weight loss during sintering of silicon–carbide whisker-reinforced alumina composites, J. Eur. Ceram. Soc. 17 (1997) 557–563.
[31] H.X. Lu, H.W. Sun, G.X. Li, C.P. Chen, D.L. Yang, X. Hu, Microstructure and mechanical properties of $Al_2O_3$–$MgB_2$ composites, Ceram. Int. 31 (2005) 105–108.
[32] S. Rajendran, H.J. Rossell, Coprecipitation-derived mullite and mullite–zirconia composites, J. Mater. Sci. 26 (1991) 5815–5822.
[33] N.C. Biswas, S.P. Chaudhuri, Comparative study of zirconia–mullite and alumina–zirconia composites, Bull. Mater. Sci. 22 (1) (1999) 37–47.
[34] C.J. Howard, R.J. Hill, B.E. Reichert, Structure of the $ZrO_2$ polymorphs at room temperature by high resolution neutron powder diffraction, Acta Crystallogr. B: Struct. Sci. 44 (1988) 116–120.
[35] P. Christel, A. Meunier, M. Heller, J.P. Torre, C.N. Peille, Mechanical properties and short-term in vivo evaluation of yttrium-oxide-partially-stabilized zirconia, J. Biomed. Mater. Res. 23 (1) (2004) 45–61.